

# PLANETARY GEAR TRANSMISSIONS LOAD SHARING MEASUREMENT FROM TOOTH ROOT STRAINS: NUMERICAL EVALUATION OF MESH PHASING INFLUENCE

J. Sanchez-Espiga, A. Fernandez-del-Rincon, M. Iglesias, F. Viadero

*Department of Structural and Mechanical Engineering, ETSIT University of Cantabria,  
Avda. de los Castros s/n 39005 Santander, Spain.*

---

## Abstract

The present work proposes a numerical approach to the problem of the calculation of the load sharing in planetary transmissions by measuring the strains in the root of the sun gear teeth, a rather common experimental procedure. The approach to model the virtual strain gauges is described in detail. This technique is modelled mimicking the experimental measuring procedure. The presented technique is employed in different simulation scenarios including in-phase and sequentially phased transmissions. Moreover, various tangential position errors are included. These configurations cover the most common scenarios in industrial applications. From these scenarios, the results show discrepancies between the real load sharing and the measured data. The nature of these discrepancies is studied in depth from the geometrical point of view.

*Keywords:* Mesh phasing, Numerical evaluation, Load sharing, Strain gauges

---

## Nomenclature

*ESIP* Equally Spaced In-Phase

*ESSP* Equally Spaced Sequentially Phased

*FE* Finite Element

*Preprint submitted to Mechanism and Machine Theory*

*April 16, 2021*

$F_{pi}$  Contact force on the planet i  
 $F_{pj}$  Contact force on the planet j  
 $LSR$  Load Sharing Ratio  
 $N$  Number of planets  
 $N_{j,i}$  Node i in section j under load  
 $No_{j,i}$  Node i in section j under no load  
 $SGLR$  Strain Gauge Load Ratio  
 $X_{p-p}^{pe}$  Peak to peak value of the strains in planet e  
 $X_{p-p}^{pf}$  Peak to peak value of the strains in planet f  
 $Z$  Number of teeth in the FE model  
 $Z_p$  Planet number of teeth  
 $Z_r$  Ring number of teeth  
 $Z_s$  Sun number of teeth  
 $\phi_i$  Planet angular spacing  
 $\theta$  Angular position  
 $\varepsilon$  Contact ratio  
 $ad$  Addendum  
 $d_t$  Mounting distance  
 $dd$  Dedendum  
 $e_t$  Tangential error  
 $h$  Depth of the local FE model  
 $m$  Module  
 $r_o$  Tip rounding arc radius  
 $wk(j)$  Number of nodes in section j

## 1. Introduction

Gear transmissions are a recurrent solution in different ambits of life. These transmissions provide a wide variety of advantages that makes them the most appropriate solution for various applications. More concretely, planetary gear trains have proved to be the best solution in order to work with high loads in a limited space, in comparison with other possible gear transmissions that normally would need of a higher size to deal with the same amount of torque. Furthermore, there exists the possibility of different speed ratios in the transmission just by changing its configuration. As a result of these advantages and several others, planetary gear trains are vastly used in sectors such as automotive industry, both in internal combustion [1, 2] and electric cars [3, 4], renewable energies [5, 6], and rotorcraft industries [7, 8].

The research and industry fields in gears have experienced a still ongoing development in the virtual world. Therefore, as years passed by, more and more models, to recreate planetary gear transmissions, have been presented. One of those is the one employed as base for this work, which was presented by Iglesias et al. in [9]. Apart from that model, in literature, countless number of them can be found in different shapes, based on different approaches, and with various levels of complexity. To name a few examples, there are lumped-parameter and purely analytical models such as [10, 11, 12, 13, 14, 15], other hybrid models with combination of FE and multibody models [5, 16] or FE and analytical approaches as in [1, 7, 17].

Despite its reduced cost and outstanding development, virtual modelling has not completely substituted experimental works in gears. There still exist numerous research works in gears from the experimental point of view, such as [18, 19, 20, 21, 22] to name a few, which prove to facilitate more accurate results in relation to the real performance of the transmission. In this scope, the study of the load sharing in planetary transmissions plays an important role, given the importance of the study of the component resistance and durability. In relation to this, different techniques have been chosen along the years to measure the load sharing in a planetary transmission. Thus, Singh et al. in [23] proposed the measuring of the load sharing by placing both root and hoop gauges along the ring gear. On the contrary, Boguski et al. proposed in [24] a new method for measuring the load on the planets by positioning strain gauges inside the planet pins. Thus, measuring the bending of the pin due to the tangential load in planet. Finally, Dai et al. [25] present a technique to measure root strains in spur planetary transmissions,

positioning the strain gauges in the sun gear.

In spite of all the studies presented above, a numerical approach to analyse the reliability of the load sharing measurements from the strains in the tooth root has been developed. This numerical approach allows quantifying the error inherent to the experimental procedure. Thus, given the fact of the need of these experimental results for the certification of the planetary gearboxes for wind turbines [18, 26], this analysis provides the opportunity to the manufacturers to quantify inaccuracies in the experimental results with respect to the real load sharing and avoid problems in terms of the durability of the components. To this aim, this work provides a numerical analysis for 3-planet planetary transmissions with different mesh phasing and tangential pinhole position errors and evaluates the discrepancies between two methods to obtain its load sharing.

Hereinafter, Section 2 presents a compilation of the relevant points for this research amongst all the aspects that compose the model presented in [9]. Also, as part of Section 2 the virtual modelling of the strain gauges (Section 2.2) is detailed and the sequence followed by the contacts in Section 2.3. Then, in Section 3 the cases of study are gathered in look for the most representative cases for the ongoing research. Finally, Section 4 gathers the results and discussion and as a consequence of those results in Section 5 some conclusions are extracted.

## 2. Modelling

In this work, a 2D spur gear planetary transmissions model, previously developed by Iglesias et al. [9], is employed and modified for the purpose of this research.

As a first step in this model, the wheels are carved applying the vectorial approach presented in [27] following the characteristics of the teeth profile. Then, the mounting of the transmission is performed. In this step, the  $\phi_i$  and the  $d_t$  are defined. As a consequence of the number of teeth in each wheel and the  $\phi_i$ , the mesh phasing is set. The classification of the transmissions regarding these details are gathered in [28]. The  $\phi_i$  and the mesh phasing play a crucial role in the transmission behaviour, as seen in [28, 29, 30]. Once the mounting is set, an example is shown in Fig.1, the input data have to be defined. Thus, the input torque, the angular positions to study, and the errors in the transmission are established. In the scope of this work only the

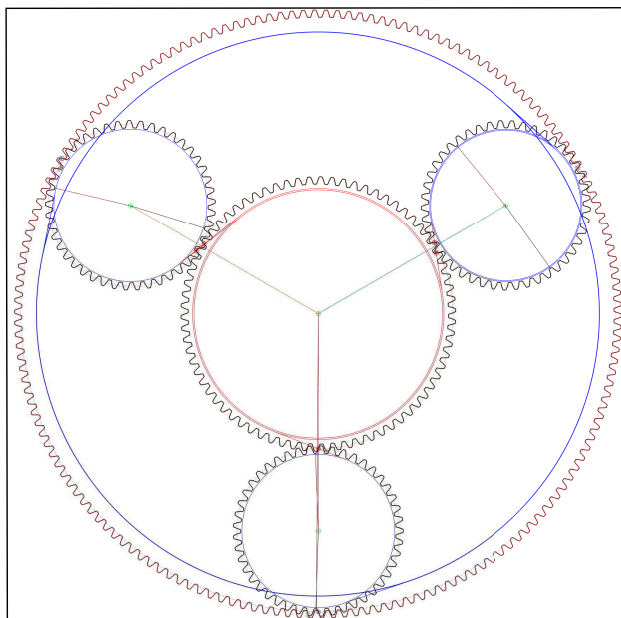


Figure 1: Mounting of the planetary transmission

tangential pinhole position error is considered, for its definition the procedure followed is analogous to the one presented in [28].

Once the mounting is finished and the input data defined, the model consists on a tool to solve the static load balance in a planetary transmission from a quasi-static point of view. This balance is found by looking for the load balance in each of the planets, and considering the load on the wheels supports in case floatability is considered. For the calculation of the balance in each wheel, it is necessary to obtain the contact forces in the interactions between wheels. In order to solve the contact problem, a hybrid formulation of analytical and FE approaches, is selected as the best option. This approach combines a pair of FE models and the analytical approach presented by Weber in [31] employed for external contact in gears, which was expanded afterwards by Iglesias et al. in [9] including internal contact too.

In terms of the FE models, there are a global model and a local model following the proposal by Brauer in [32], these models for the sun gear are shown in Fig.3. The first reproduces the body of the wheel and a  $Z$  number of teeth, this point will be explained in more detail in section 2.1. Secondly, the local model provides a FE model of the active flank with an  $h$  depth, which was determined in [9]. The load applied in both of the models is unitary and

has the opposite direction, thus, by summing the results up the distortion in the tooth flank due to the point force is erased. Likewise, the deflection of the teeth and the body of the gear are calculated for such unitary force. Then, this scenario is repeated for any load case along the flank of the tooth. Thus, the flexibility of the wheel is obtained. The next step consists on using the analytical approach to calculate the deformations in the local area due to a Hertzian load on the flank. This last step is iterated looking for convergence. Finally, all these steps are combined, by using the superposition principle [32], to obtain the deflections in the teeth due to the load.

At the same time, the geometry of the wheels is employed to calculate the overlap between teeth, supposing that the profiles are rigid and that they are allowed to overlap. Thus, the possible contacts are calculated and the actual contacts correspond to those where the overlap exists. These possible contacts are illustrated in Fig.2 and the number of them that are considered depend on the contact ratio, as it will be explained in more depth in section 2.1. Finally, relating the stiffness obtained from the deflections and the overlaps, the contact forces are obtained.

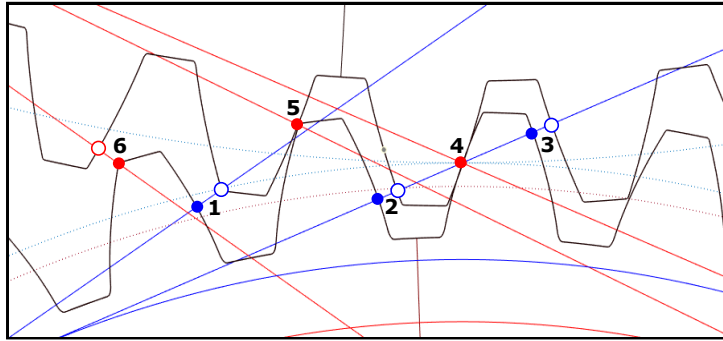


Figure 2: Contact between sun-planet

From the contact forces, firstly, the balance in each planet is searched. Once the balance in every planet is attained, there should also exist a balance in the whole transmission. To that aim, given the lack of angular acceleration and the friction or damping losses, the input torque should equal the output torque that planets induce on the planet-carrier. This stands for configurations such as the studied, where the fixed member is the ring gear.

Once the balance is attained and the contact problem is solved, the immediate load sharing amongst the planets can be calculated for any angular position, by following the procedure defined in section 2.4.

### *2.1. Finite-element Models*

As mentioned before, the contact problem employs a hybrid point of view. The FE models employed in this approach consist on a global and a local FE models shown in [9, 28]. For this work, the information is extracted from the global model, presented in Fig.3a. The measuring of strains in the sun gear root is a technique employed in some cases [18, 25]; this is the preferred procedure whenever the sun gear is big enough to dispose the gauges and necessary telemetry. In addition, these measurements are necessary in order to certify the gearbox, at least in the wind generators business. However, this represents one possibility, another possible technique consists on measuring the strains in the ring gear, at least for flexible rings such as the ones presented in [23, 33].

This model is developed using the partial differential equation toolbox in MATLAB. It is a 2-D model discretized by using triangular elements with nodes only at every vertex. Although the model creates FE models for every gear, in this work the focus will be set on the sun gear, and this will be the only FE model referred from now on. In the FE model, apart from the gear body a  $Z$  number of teeth is represented. In relation to the boundary conditions, the nodes along the inner circle, where the gear is mounted on the shaft, are embedded. The rest of the nodes and elements are free in the plane.

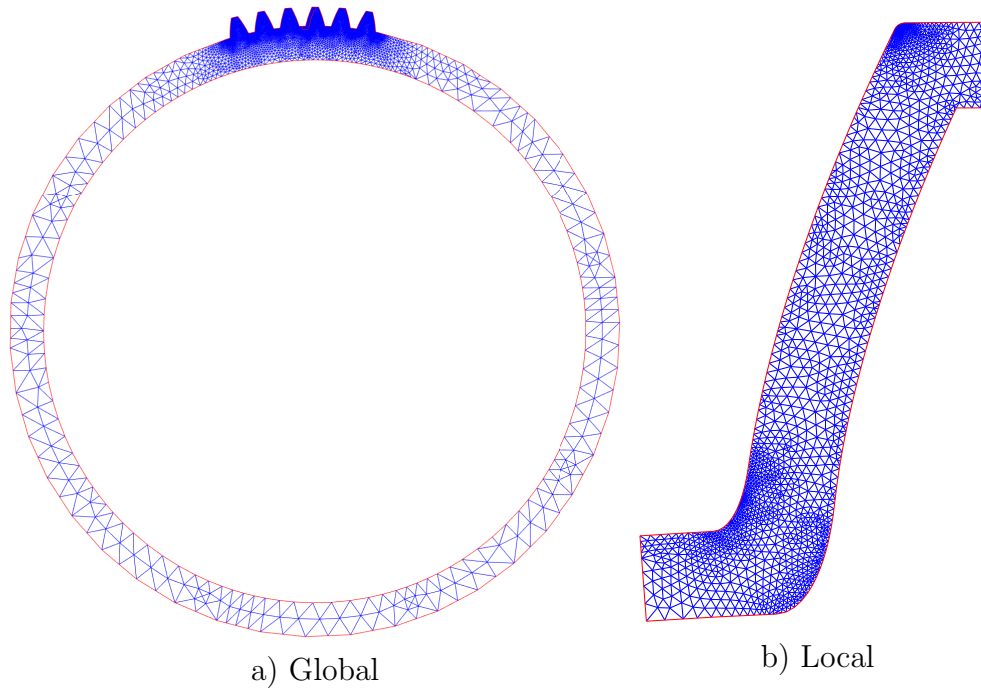


Figure 3: FE models for the sun gear

Going back to the  $Z$  number of teeth in the model, this is obtained by using (1). The  $Z$  number considers all the possible contacts given the contact ratio (Fig. 2), and gathers the teeth that suffer strains due to the contact and also all the adjacent teeth affected by that contact. Also, this expression accounts for high contact ratio spur gears.

$$Z = 2 \cdot \text{Ceil}(\varepsilon + 1) \quad (1)$$

In equation (1) the function  $\text{ceil}$  rounds the  $\varepsilon+1$  to the next integer in the positive direction. For the simulations performed in this work,  $Z$  will be equal to 6, given the contact ratios specified in Tab.3.

Table 1: Theoretical contact ratios in the studied configurations

Configuration	Parameter	Value
ESIP	Contact ratio (sun-planet)	1.294
	Contact ratio (planet-ring)	1.395
ESSP	Contact ratio (sun-planet)	1.295
	Contact ratio (planet-ring)	1.397

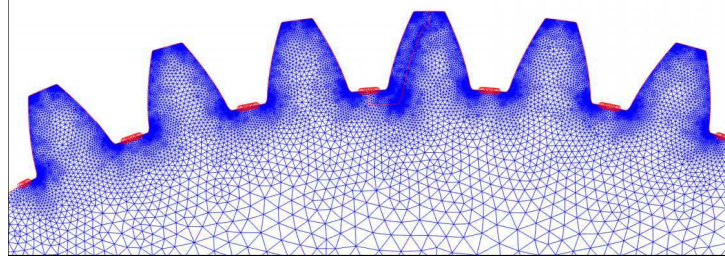
### 2.2. Virtual strain gauges

In the following, the modelling of the virtual strain gauges is described. This approach obtains the strains in the root of the sun gear teeth by processing the already existing information in the global FE model. Thus, the change in the distance between adjacent nodes in different sections is obtained using (5). The first step to take consists on identifying in the FE model the nodes that are relevant, select them and gather the coordinates of their initial position. For this, three conditions are established:

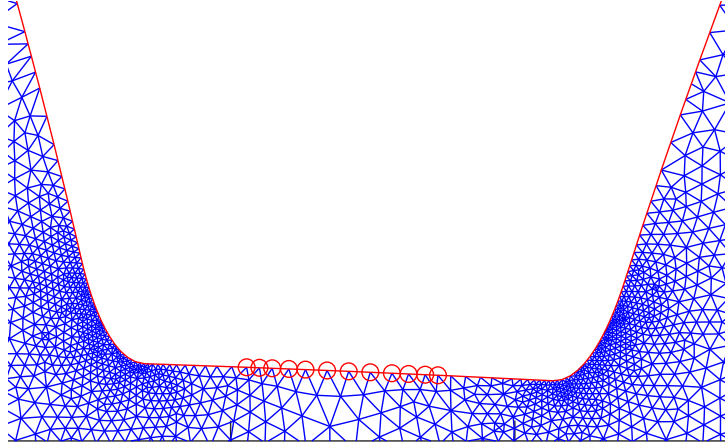
- The nodes have to belong to the root circumference.
- They must be in the arc that connects the trochoids of consecutive teeth, but avoiding the nodes along the trochoid.
- At the first and last teeth this number of nodes just have to be on the root circumference.

Avoiding the trochoid of the teeth profile, the stress concentration effect that appears in this zone with the load would be avoided. Therefore, the strain gauge data will not be distorted by such effect. Taking all the previous into account, the nodes selected appear in Fig.4 and their coordinates are stored. Thus, the initial position of the nodes of interest is monitored. In this initial configuration no load is applied in any of the  $Z$  teeth. By this procedure, the number of noded sections where the strains are measured will be  $Z+1$ , always.

Secondly, in order to establish the initial length of the strain gauge each section of nodes is analysed separately. In every section, the distance between each pair of consecutive nodes is calculated by using (2). This equation approximates the distance as a straight line, a good enough approximation given the reduced length and therefore the negligible curvature.



a) Z teeth



b) Root between teeth

Figure 4: Detail of the selected nodes.

$$\overline{No_{j,i}No_{j,i+1}} = \sqrt{(No_{j,(i+1)x} - No_{j,ix})^2 + (No_{j,(i+1)y} - No_{j,iy})^2} \quad (2)$$

The subindexes x and y identify the horizontal and vertical components of the nodes Cartesian coordinates.

The summation of the distances between the nodes that belong to each of the sections provides the length of the strain gauge. Equation (3) provides the reference value of that length whenever there is no load in the model.

$$Lo_j = \sum_{i=1}^{wk(j)-1} \overline{No_{j,i}No_{j,i+1}} \quad (3)$$

Then, equation (4) provides the results for the same calculation when load is applied in the model. The lack of the subindex o in the equation identifies this detail.

$$L_j = \sum_{i=1}^{w_k(j)-1} \overline{N_{j,i} N_{j,i+1}} \quad (4)$$

Once these values are known, the strain in each of the monitored sections will correspond to the difference in length of each section between the unloaded and the loaded configuration (5).

$$\Delta L_j = L_j - L_{o_j} \quad (5)$$

With the previous steps, the strains in a supposed strain gauge could be model, and the strain gauge positioned in any of the monitored sections. However, in order to obtain the measurements of a strain gauge placed in one of the sections of nodes monitored, it is important to define the acquisition sequence, and to take into account the effect of any contact on such strain gauge. In the following section, all of this is explained.

### 2.3. Contact sequence

In order to manage the information acquired by the strain gauge its location is greatly relevant. The strain gauge is considered to be positioned in the  $(Z/2)+1$  section, which is the midst of the model. Thus, the initial single contact in the first tooth will have a small, but notable, influence on the gauge. As commented before, the number  $Z$  of teeth show all the teeth that are notably influenced by a contact on the middle tooth. Consequently, the gauge placement assures the measuring of the strains produced by any contact in any of the considered teeth.

Thus, the contact sequence starts with a single contact in the first tooth, which will produce a small strain in the gauge. After this, the contact will continue to the point that there will appear a double contact both in the first and second tooth. In such scenario, firstly, the strains due to the first contact will be monitored and, then, the ones due to the second. Finally, the superposition principle will sum up the effects of both contacts. This strategy will be applied continuously during the  $Z$  meshing cycles in the  $Z$  teeth, considering every possible contact that affect the strain gauge.

In Fig.5, the contact sequence for the cases considered in this work is presented. The snapshots for simple and double contact are represented. Every snapshot includes the strain gauge representation by a thick red line between teeth 3 and 4.

In order to virtually recreate what is presented in Fig.5, the strains in every section between teeth are calculated in every contact position. Then,

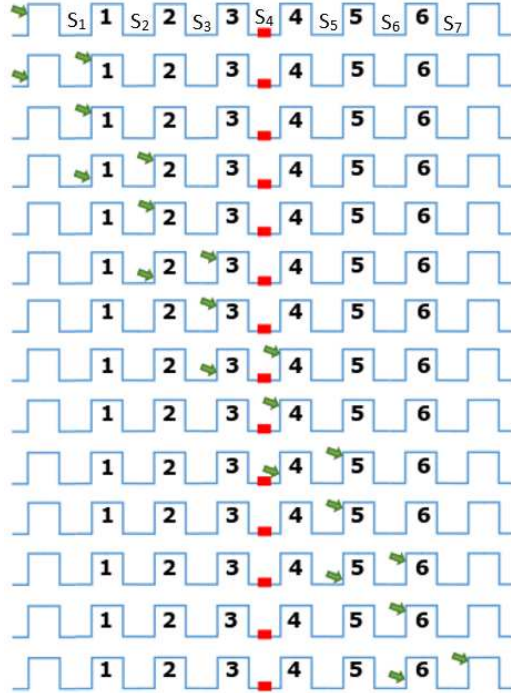


Figure 5: Snapshots of the contact sequence for single and double contact

due to the employed model, the relative position of the contact has to be taken into consideration to obtain the strain in the gauge. For instance, the contact in the first tooth considered would relate to the strain obtained in the last of the noded sections. As contacts continue, the strains that are considered change from one section to the next whenever the tooth where the contact appears changes too. After repeating this procedure for every contact position in each of the considered meshing cycles, the whole sequence of strains in the gauge is determined.

Finally, it is necessary to point out that for the simulations performed for this work, 8 meshing cycles in the sun gear have been considered. As expressed before, at least  $Z$  meshing cycles are necessary, in this case,  $Z$  equals to 6. However, the sequentially phased configuration includes a delay in the contacts between consecutive planets, which makes necessary considering a higher number of meshing cycles. In conclusion, by measuring the strains in 8 meshing cycles for every case of study, the acquisition of all the crucial information in terms of strains is assured.

#### 2.4. Load sharing calculation

In this work, the load sharing amongst planets will be calculated employing different definitions.

Firstly, for the immediate calculation of the load sharing, the LSR is the magnitude chosen. This was employed previously in [28, 34], also referred as Load Sharing Factor (LSF) in [1, 24, 35]. This LSR allows to observe the amount of load in each planet, compared to the inlet torque at any moment of the simulation. The analytical definition of the LSR appears in equation (6). The load sharing by this definition is calculated as the amount of load in a planet  $e$  divided by the total load in all the planets. This calculation is performed whenever the static balance is attained in the whole transmission.

$$LSR_{p_e} = \frac{F_{p_e}}{\sum_{f=1}^N F_{p_f}} \quad (6)$$

In order to address the differences between the calculation of the load sharing by using the LSR and the strain measurements Fig.6 & Fig.7 are included. These represent ideal scenarios of the behaviour of both ESIP and ESSP transmissions without any tangential error in the pinhole of the planets. A sketch of the LSR and the strains in the gauges shows this behaviour. In both figures, the LSR is a continuous calculation. On the contrary, the strains in the contact with each planet are measured during a period of time. In each of the measurements of strains, the peak-to-peak value in the strains is obtained.

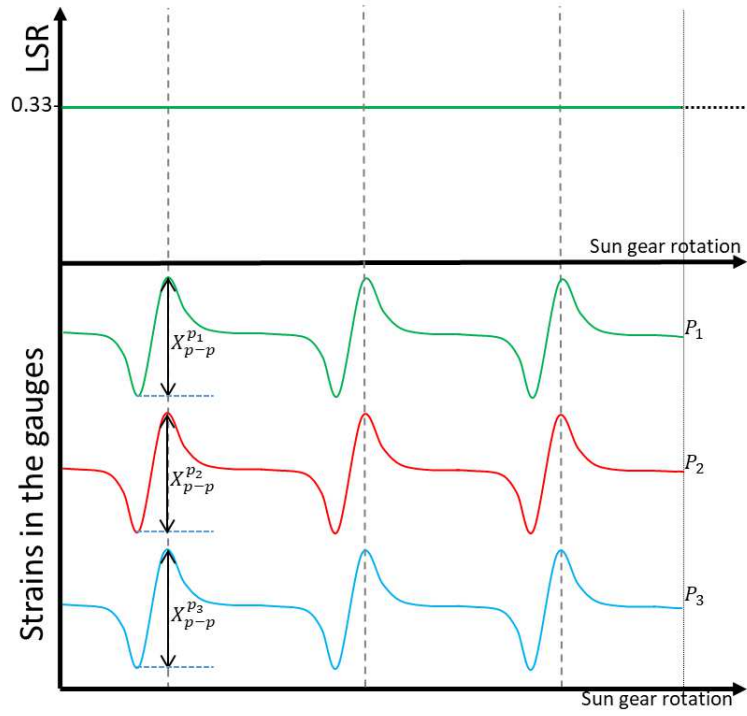


Figure 6: Comparison of the LSR and the strain measurements in the ESIP transmissions

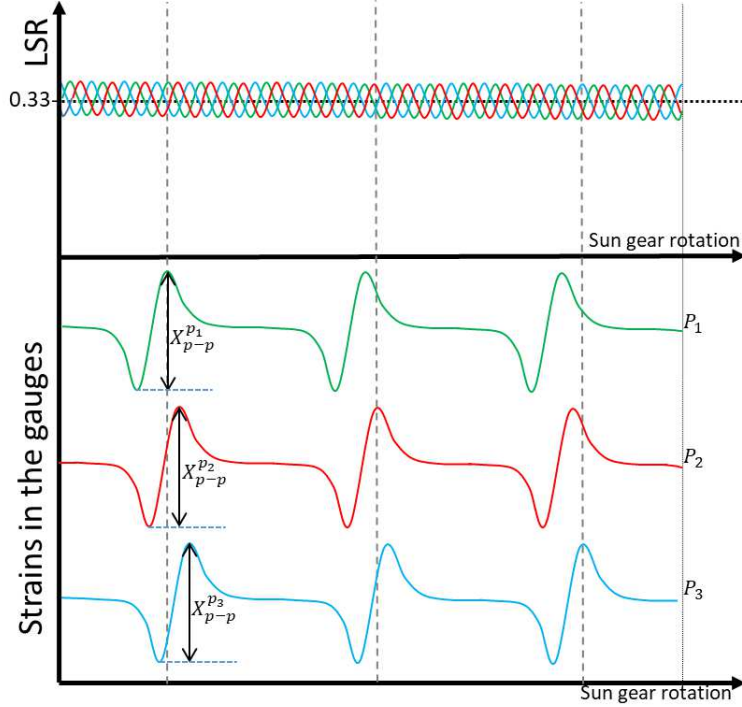


Figure 7: Comparison of the LSR and the strain measurements in the ESSP transmissions

As seen in Fig.7, there exists a synchronicity between the peaks in the LSR and the strains. The maximum level of load, signalled by the maximum in the LSR, coincides with the peak of peak-to-peak value in the strains. After this, the calculation of the load sharing from the strains, which will be referred in the following as SGLR, is calculated. This magnitude refers to the size of each peak-to-peak value compared to the total of summation of every peak-to-peak value. Thus, the peak-to-peak value corresponding to each planet will be the same and will lead to a uniform result in the SGLR. On the contrary, a transmission with a sequential mesh phasing will have a fluctuating LSR, different to the SGLR as seen in Fig.6. Thus, the SGLR will only coincide with the real load sharing in the transmission in the ideal scenario of an ESIP transmission without any error, as seen in Fig.6. In order to obtain the SGLR (7) is used.

$$SGLR_{pe} = \frac{X_{p-p}^{pe}}{\sum_{f=1}^N X_{p-p}^{pf}} \quad (7)$$

In equations (6) & (7) the subindex f is used as an auxiliary subindex to sum up the contributions of every planet in the transmission.

### 3. Cases of study

Hereinafter, the cases of study considered to analyse the measuring of the load sharing in various configurations of planetary transmissions are compiled. The load sharing is obtained both by the calculation of the LSR and also by the measurements using virtual strain gauges, and the consequent calculation of the SGLR.

In this work, the focus is on the mesh phasing and the effect of the pinhole tangential position error. In every transmission, the planets will be equally spaced, and in terms of phasing there will be in-phase (ESIP) and sequentially phased (ESSP) transmissions. To this aim, the number of teeth considered for each gear is gathered in Tab.2. These configurations respond to the most common configurations employed in planetary transmissions for wind generators [5, 20, 36].

Table 2: Number of teeth for each gear in the considered transmissions

	$Z_r$	$Z_p$	$Z_s$
ESIP	165	44	75
ESSP	166	45	74

In more depth, in Tab.3 the geometrical characteristics of the teeth are compiled apart from the number of teeth. The geometry of these profiles includes a tip rounding arc to avoid problems due to the contact on the edges.

Table 3: Geometrical specifications of the teeth profiles

Parameter	Value
Module (mm)	4.5
Pressure angle ( $^\circ$ )	20
Addendum	1·m
Dedendum	1.25·m
Tip rounding arc radius (mm)	0.05·m

Apart from the effect of the mesh phasing, seven sizes for tangential pinhole position error are considered. Every possible combination in terms of phasing and errors are gathered in Tab.4. These will be the cases considered for the simulations in this work. For every scenario a torque of 1200 Nm is applied counter-clockwisely.

Table 4: Compilation of the studied scenarios

Configuration	Tangential error						
ESIP	0 $\mu\text{m}$	1.25 $\mu\text{m}$	2.5 $\mu\text{m}$	3.75 $\mu\text{m}$	5 $\mu\text{m}$	6.25 $\mu\text{m}$	7.5 $\mu\text{m}$
ESSP	0 $\mu\text{m}$	1.25 $\mu\text{m}$	2.5 $\mu\text{m}$	3.75 $\mu\text{m}$	5 $\mu\text{m}$	6.25 $\mu\text{m}$	7.5 $\mu\text{m}$

None of the mentioned configurations include flexibility in the shafts that support the wheels. This decision is due to the need of observing the pure effect of the load in the transmission and in the strain measurements, to which aim, the lack of floatability is a great asset. Nonetheless, in a future further step, the focus should be on the inclusion of floatability in the gear supports, increasing the realism of the simulations. However, it is important to highlight the importance of this consideration knowing that a more rigid system is more sensitive to any error, as it can be seen in [37] where the stiffness is increased by augmenting the  $N$ . This effect will probably be seen whenever the radius of the shaft mounting is modified, or the geometry of the teeth, or even the number of teeth. Thus, leading to a more rigid system more sensitive to errors, which translate in higher imbalances for a given error.

#### 4. Results and discussion

Hereinafter, the results to the cases of study are summarised. As a first step to comprehend the obtained results, Fig.8 & Fig.9 present the detail of sun-planet contacts, where the contacts are highlighted by a red circle and numbered as presented in Fig.2. In the in-phase configuration only one figure is presented given the fact that every contact is at the same situation for any of the planets. These figures prove the differences in the contacts due to the mesh phasing. Both configurations are ideally perfect, therefore, the difference in the pairs of teeth in contact is caused by the mesh phasing.

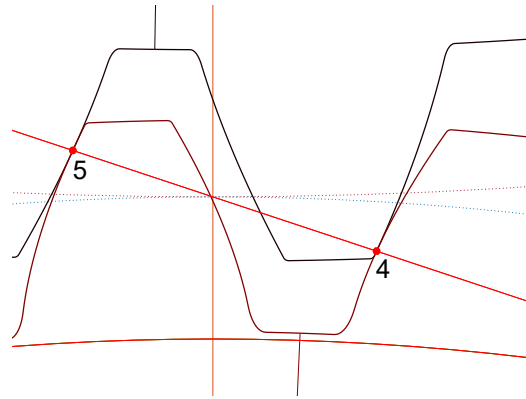


Figure 8: Detail of the sun-planet contact in the initial position for ESIP transmission

On the contrary, in a sequentially phased transmission every contact is at a different point along the meshing line, as seen in Fig.9. Thus, the number of teeth pairs in contact varies from one planet to the other. Likewise, the meshing stiffness varies in each of the contacts and will influence the load sharing and the strains.

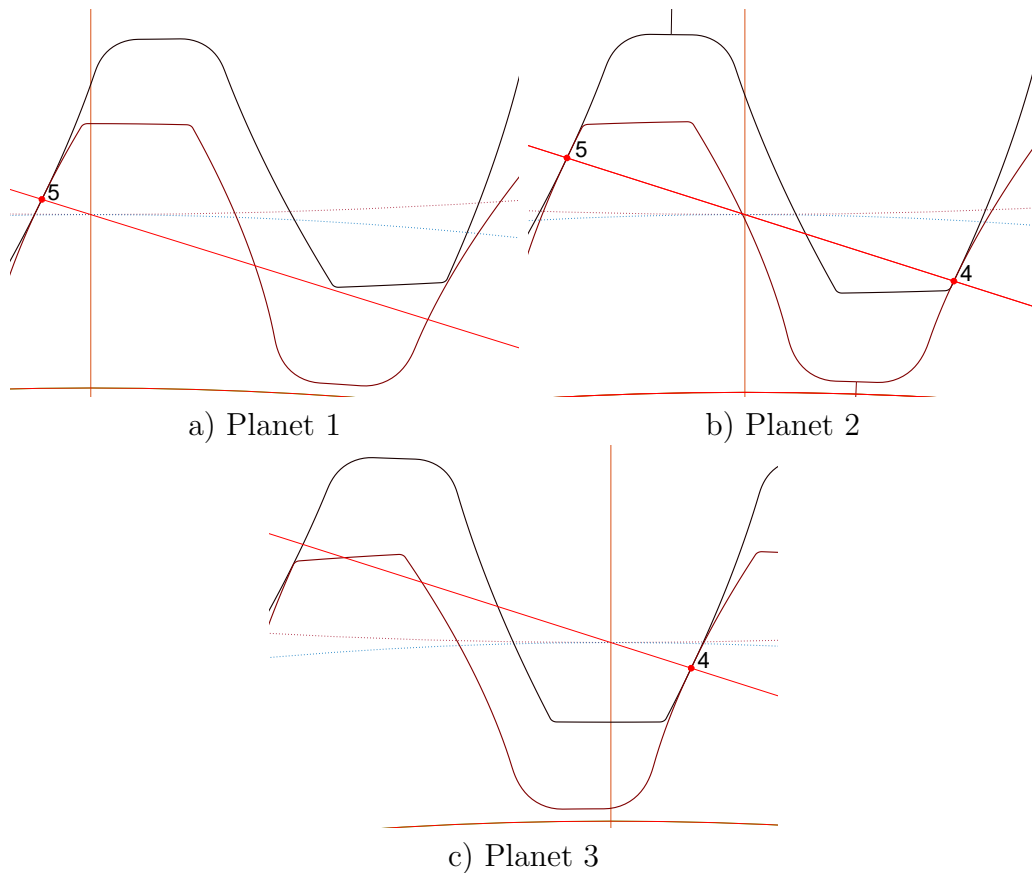


Figure 9: Detail of the sun-planet contact in the initial position for ESSP transmission

As a consequence of those differences in the contacts, in Fig.10 a series of mechanical scenarios are plotted in order to introduce the physical explanation for the obtained results. Thus, the figure shows snapshots of 3 instants throughout the simulations. In every instant a blue dotted box shows the stiffness observed in the contact on each planet. This stiffness is related directly with the contact forces and the strains suffered by the strain gauge. Besides, this stiffness is affected by the mesh phasing. Then, given the data in each of these instants, considering the peak-to-peak value proportional to that stiffness, the SGLR is induced.

As shown in Fig.10, the springs present differences in stiffness due to the mesh phasing in the sequentially phased scenario. For the strains experienced by the strain gauge, the differences due to the mesh phasing are not visible given the fact that the same cycle is repeated for every contact at different

moments along the simulation. Although the cycles in the strains are not affected by the mesh phasing, it is notable for the LSR in each of the instants. Given that, discrepancies are expected between the results obtained by using each of the proposed techniques. This is a consequence of the fact that the strain gauge only observes what happens in each planet, and not on the rest, for a period of time, but whenever the sun will reach every different planet will observe analogous conditions. However, the LSR observes the circumstances in every planet at the same time, and therefore, it is affected directly by the conditions in the whole transmission and not only in one of the planets as it happens with the SGLR.

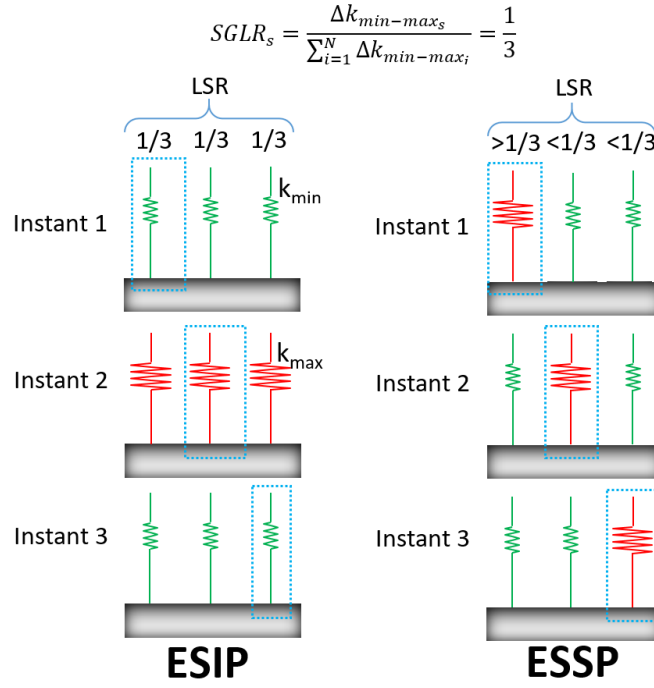


Figure 10: Spring comparison in snapshots for the LSR and SGLR discrepancies without errors

In order to observe in detail the magnitudes mentioned in section 2.4, the LSR is presented, together with the strain measurements. This is presented for the case where there is a tangential position error of  $1.25 \mu\text{m}$ . These magnitudes are shown both for the in-phase (Fig.11) and sequentially phased (Fig.14) transmissions. By using this scenario, all the effects can be analysed and explained. Later, the results for all the other cases studied are presented

together in order to show the tendencies that can be identified both in the LSR and the strains measurements.

Regarding the strains measured in the root of the teeth in the sun gear, these are shown in Fig.11 for the ESIP transmission with a  $1.25 \mu\text{m}$  tangential error. Given the applied torque and the direction of the rotation in the sun gear, the contacts in the successive teeth start by compressing the gauge. The closer the contact gets to the gauge, the higher the measured compressing strain. However, whenever the contact becomes a double contact both in the tooth before and after the strain gauge, there is a combination of traction and compression that leads to the tipping point located right after the 4<sup>th</sup> meshing cycle in the sun. In the meshing cycles afterwards, the strains are tractions in the gauge whose amplitude diminishes as the meshing continues, given the fact that the contacts happen further from the gauge. As seen in the lower graph in Fig.11, due to the tangential error included in the mounting of the planet 1, the amount of load in this planet is lower than in the other planets, as it can be expected in these conditions. For in-phase transmissions, this error affects equally the planet 2 & 3, therefore, the behaviour of the LSR and strains in planets 2 & 3 are perfectly identical, that is the reason why these lines overlap. Besides, the error in the planet 1 translates also in a lower peak-to-peak value in the strains due to the contact with this planet. At the same time, the error narrows the width of the different strain sections in the strain graph in the planet 1. This narrowing is visible in the moment when the slope in the graph changes. This narrowing is due to the lower load in that planet together with the flexibility of the tooth, which leads to a lower effective contact ratio in that planet compared to the rest.

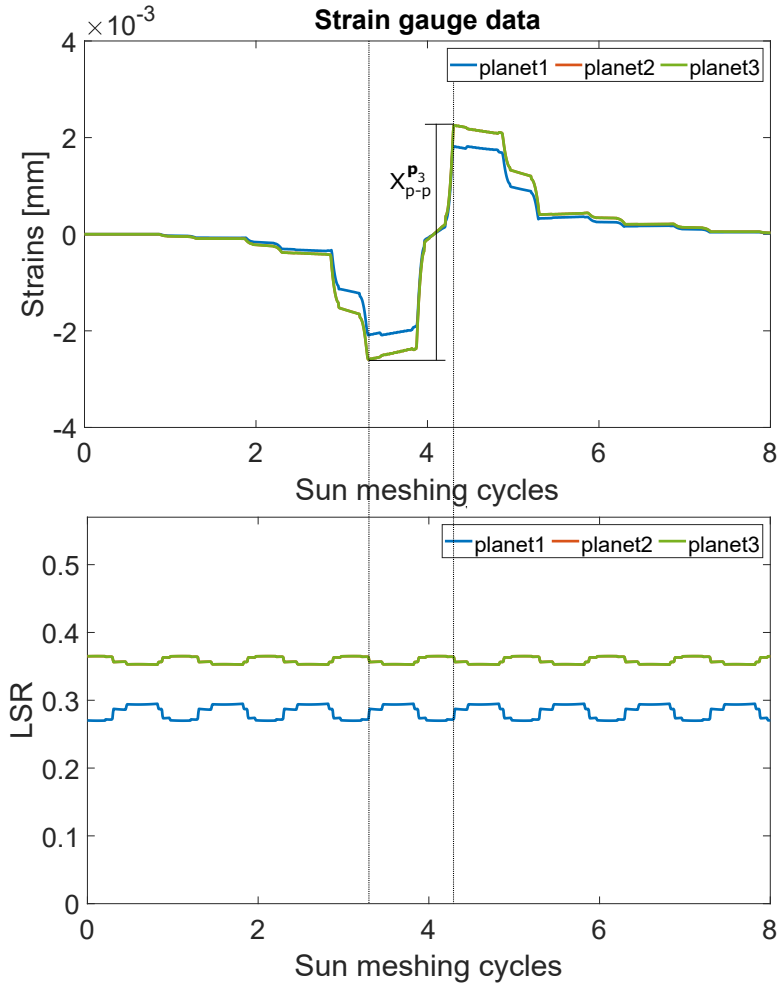


Figure 11: LSR and strain measurements ESIP@ $e_t[1,25]$

Whenever the results in the strain measurements are observed together with the LSR results more effects can be identified. In Fig.11 some dotted lines are included in order to show the synchronicity in a relevant event such as the peak values in the strains and in the LSR. The changes in the LSR are related with the changes in the meshing stiffness, as well as the change of the pairs of teeth in contact. The inexistence of mesh phasing makes this changes synchronous in each planet except for the small delay in the planet 1 due to the tangential error. In terms of the LSR, the variations in the planet 1 inside a meshing cycle are bigger than in the other planets. However, the average load in this planet is lower than in the rest of planets and, thus, the

strains are smaller.

These effects are studied in more depth varying the size of the tangential error in the mounting of the planet 1, as seen in Fig.12 & Fig.13. Thus, the variation of this error creates a tendency that continues along the simulations and prove the effects commented before. The higher the error, the bigger the imbalance in the LSR, and the lower the load in the planet with the error. Because of that, the lower the strains in the contact with that planet. At the same time, the impact of the error in the width of the events in the strains and LSR becomes more visible the higher the error, proving what was commented but was difficult to spot for the case with 1.25  $\mu\text{m}$  error.

In Tab.5, the numerical results to the magnitudes of interest are gathered. In this case, the lack of mesh phasing uniforms the results in the maximum LSR (Max. LSR) and in the SGLR. This uniformity continues in the cases where there is tangential error in the planet 1. Even though there is an error, planets 2 & 3 conserve the uniformity in the mentioned results. Apart from that, the numerical results prove that the measuring of the strains to calculate the load sharing tend to minimise the impact of the tangential error. Thus, the SGLR in the planet 1 is higher than the average LSR, as well as the SGLR in planets 2 & 3 is lower than the average LSR. Therefore, the load sharing obtained in the SGLR is more uniform and diminishes the impact of the tangential error.

Table 5: Numerical results for the ESIP transmission in every case of study

$e_t$ ( $\mu\text{m}$ )	Planet 1			Planet 2			Planet 3		
	Avg. LSR	Max. LSR	SGLR	Avg. LSR	Max. LSR	SGLR	Avg. LSR	Max. LSR	SGLR
0	0.333	0.333	0.333	0.333	0.333	0.333	0.333	0.333	0.333
1.25	0.2829	0.2949	0.2872	0.3586	0.3651	0.3564	0.3586	0.3651	0.3564
2.5	0.2328	0.2564	0.2465	0.3836	0.3967	0.3767	0.3836	0.3967	0.3767
3.75	0.1834	0.2179	0.2076	0.4083	0.4281	0.3962	0.4083	0.4281	0.3962
5	0.1346	0.1796	0.1688	0.4327	0.4592	0.4156	0.4327	0.4592	0.4156
6.25	0.0869	0.1413	0.1309	0.4566	0.4897	0.4345	0.4566	0.4897	0.4345
7.5	0.0516	0.1035	0.0935	0.4742	0.5	0.4533	0.4742	0.5	0.4533

On the other hand, for ESSP configurations, as shown before in Fig.9 the contacts in each of the planets differ. Thus, the meshing stiffness is different and also will be the LSR and the strains, as shown in Fig.14. The mesh phasing provokes a delay between the peak values in the LSR. Then, the error adds a little difference in the behaviour of the planets, a tangential error equals to a small delay in the mesh phasing, thus, the peak values in the LSR are not equal to each other. However, in the configuration without

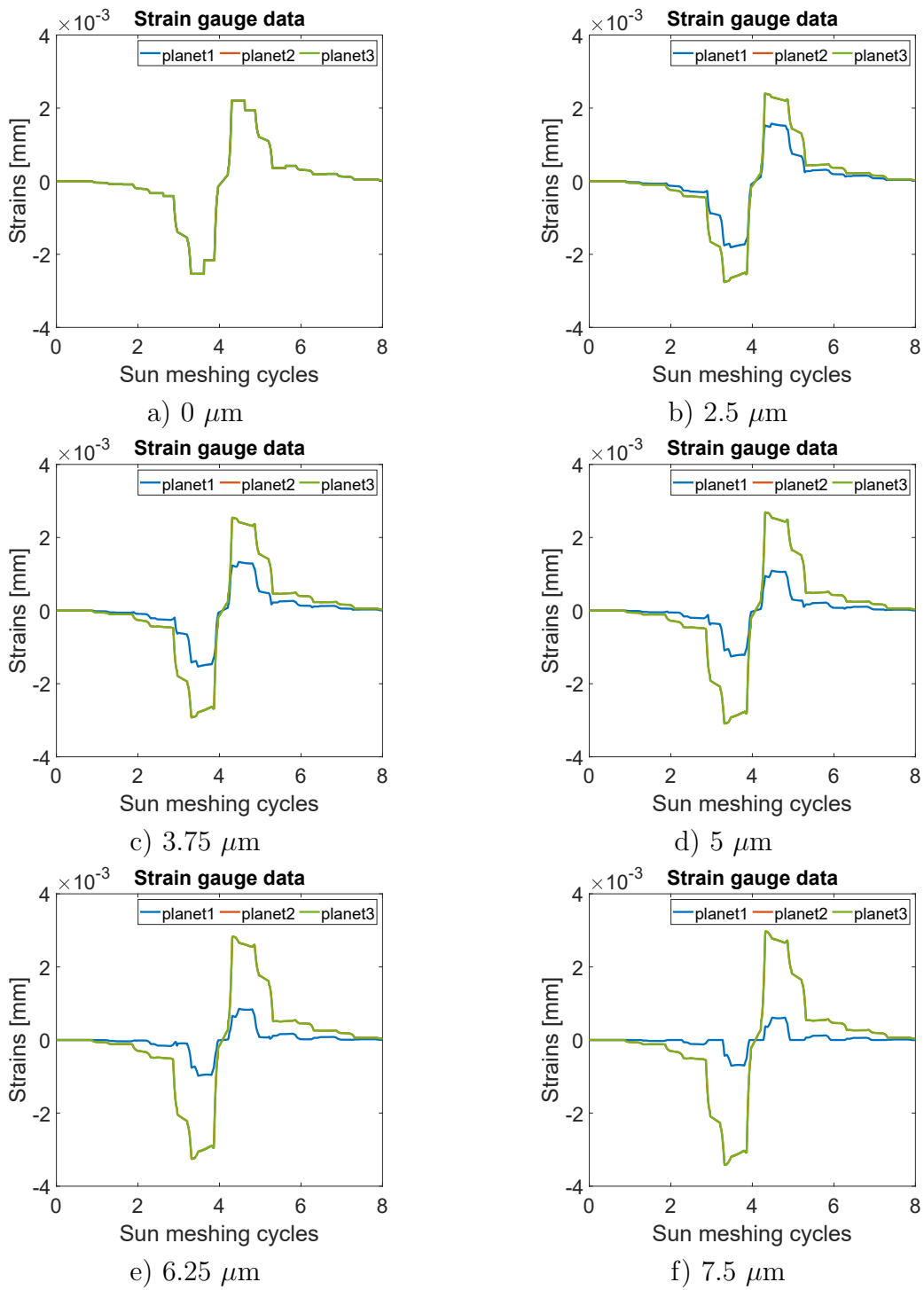


Figure 12: Strain gauge data in ESIP with various errors

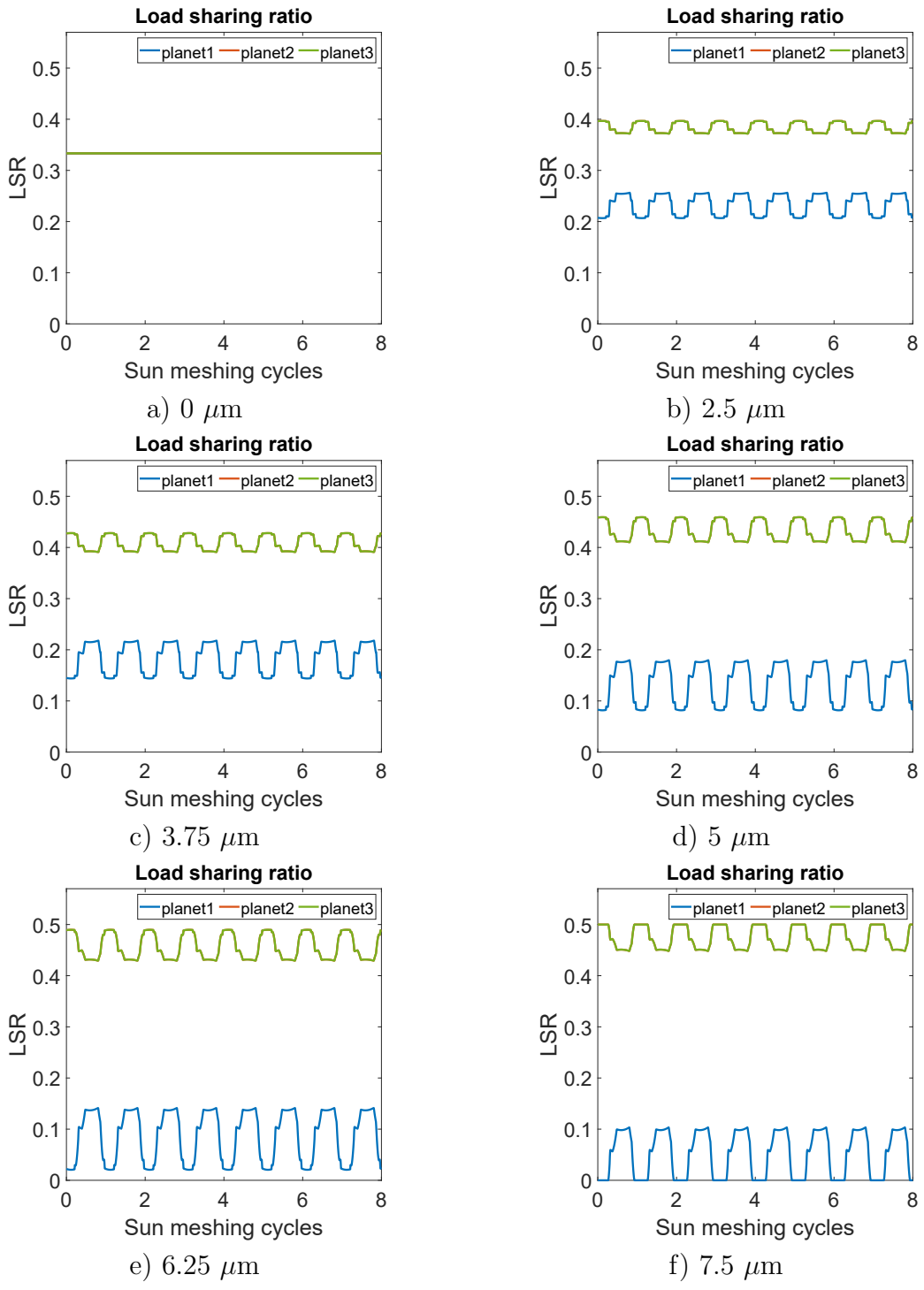


Figure 13: Load Sharing Ratio in ESIP with various errors

error the peak values are identical. Later, relating the strain measurements and the LSR, it is visible how there is a synchronicity between the peak values in the LSR and in the strains, and how these peaks are separated by the mesh phasing. Besides, the peak values of the strains in each planet are not identical either. Thus, the error modifies the geometry of the contact and the situation where the highest strain appears in any planet is not equal to the others.

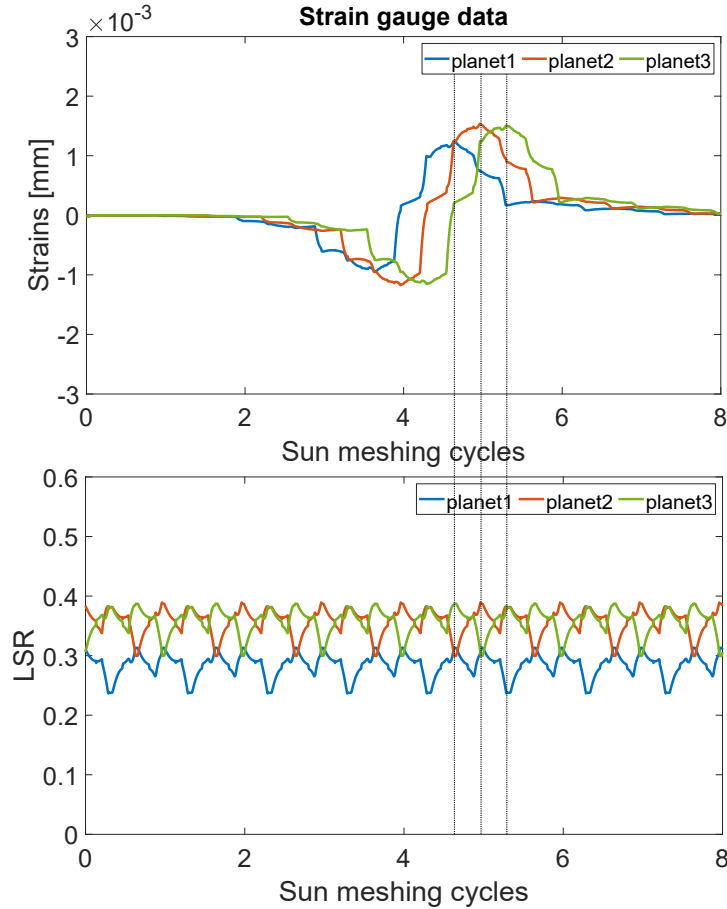


Figure 14: LSR and strain measurements ESSP@ $e_t[1,25]$

However, this difference is purely due to the tangential error. In Fig.15 & Fig.16 in the case without error every peak is identical to the rest, but the bigger the error, the bigger the difference between these peaks. This effect is due to the modification of the sequential phasing. The mesh phasing in a

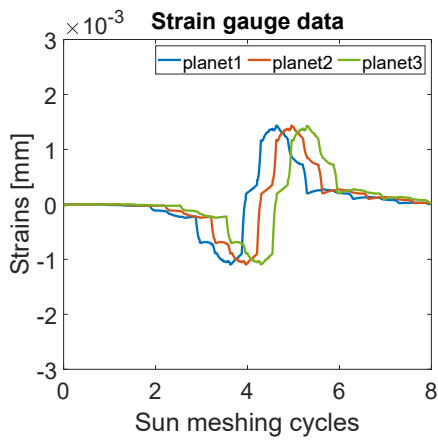
sequential configuration is uniformly divided in  $N$  parts. A tangential error modified this division and, thus, each contact affects the rest but not equally, therefore, an imbalance is created and the load in each of the planets will not be the same. This stands also for the strains, given the fact that they are a direct consequence of the contact forces. The numerical values extracted from these results are gathered in Tab.6.

The numerical results gathered prove how these measurements tend to diminish the influence of both the mesh phasing and the tangential error. Thus, the results of the SGLR prove to be more uniform than the maximum values in the LSR. Thus, SGLR overestimates the uniformity in the load balance in the ESSP transmission studied.

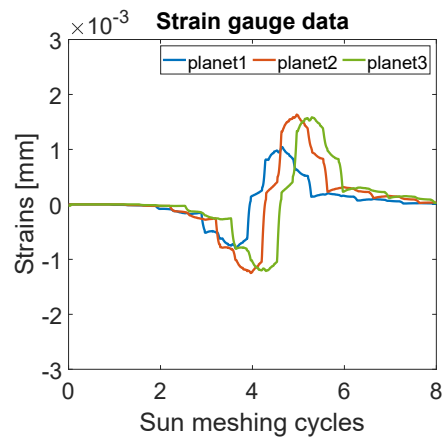
Table 6: Numerical results for the ESSP transmission in every case of study

$e_t$ ( $\mu\text{m}$ )	Planet 1			Planet 2			Planet 3		
	Avg. LSR	Max. LSR	SGLR	Avg. LSR	Max. LSR	SGLR	Avg. LSR	Max. LSR	SGLR
0	0.333	0.363	0.333	0.333	0.363	0.333	0.333	0.363	0.333
1.25	0.2844	0.3136	0.2888	0.3579	0.3893	0.3585	0.3578	0.3875	0.3527
2.5	0.2358	0.266	0.2446	0.3822	0.4142	0.3833	0.3821	0.4179	0.372
3.75	0.1877	0.2188	0.2011	0.4062	0.4407	0.4078	0.4062	0.4485	0.3911
5	0.1401	0.1719	0.1562	0.4299	0.467	0.4303	0.43	0.4776	0.4135
6.25	0.0933	0.1251	0.1106	0.4533	0.4931	0.453	0.4534	0.5061	0.4364
7.5	0.0475	0.0769	0.0656	0.4761	0.517	0.4753	0.4764	0.5344	0.459

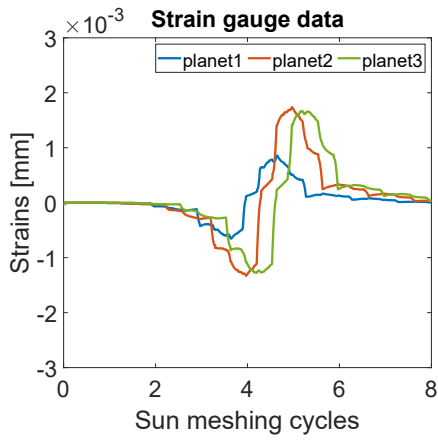
In a further step, the tendencies of the inaccuracies between the real maximum of the load sharing, obtained from the LSR, and the load sharing obtained by the SGLR are represented in Fig.17. This figure gathers the maximum value of these discrepancies. In this scenario, it is important to observe the fact that in the in-phase transmission without any error, the existing ideal balance leads to an accurate calculation of the load sharing with the SGLR. However, in the same scenario but with sequential phasing, there exists a discrepancy between the LSR and the SGLR. Thus, the accuracy of the load sharing calculated from the strain measurements is quantified. Then, the increment of the tangential error in the planet 1 mounting increases these inaccuracies. In terms of the growth of the inaccuracy in the calculation of the load sharing, in the ESIP configuration this pace seems to be uniform for any tangential error until the  $7.5 \mu\text{m}$  tangential error that produces moments where the contact in the planet 1 is lost, as seen in Fig.13f. On the contrary in the ESSP transmission this pace varies with the tangential error and different slopes can be identified in the graph. The variation between the scenarios with 0 error and 1.25 present a slight variation, however, in the scope from



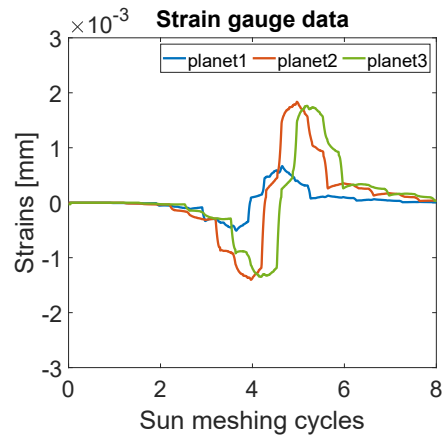
a)  $0 \mu\text{m}$



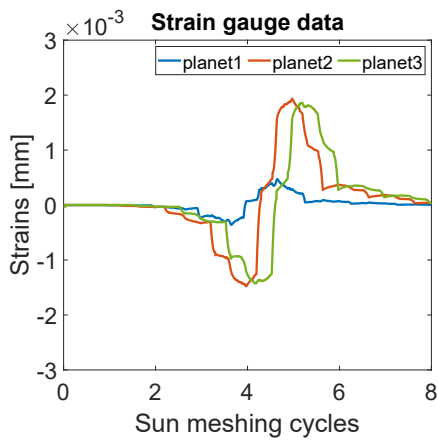
b)  $2.5 \mu\text{m}$



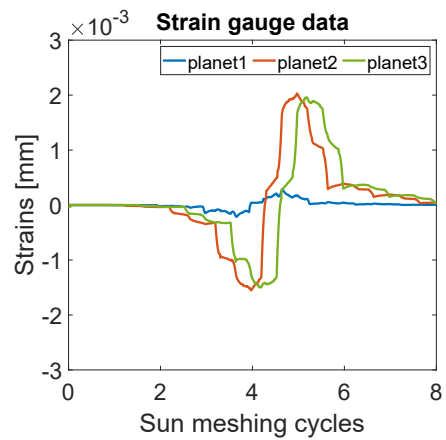
c)  $3.75 \mu\text{m}$



d)  $5 \mu\text{m}$



e)  $6.25 \mu\text{m}$



f)  $7.5 \mu\text{m}$

Figure 15: Strain gauge data in ESSP with various errors

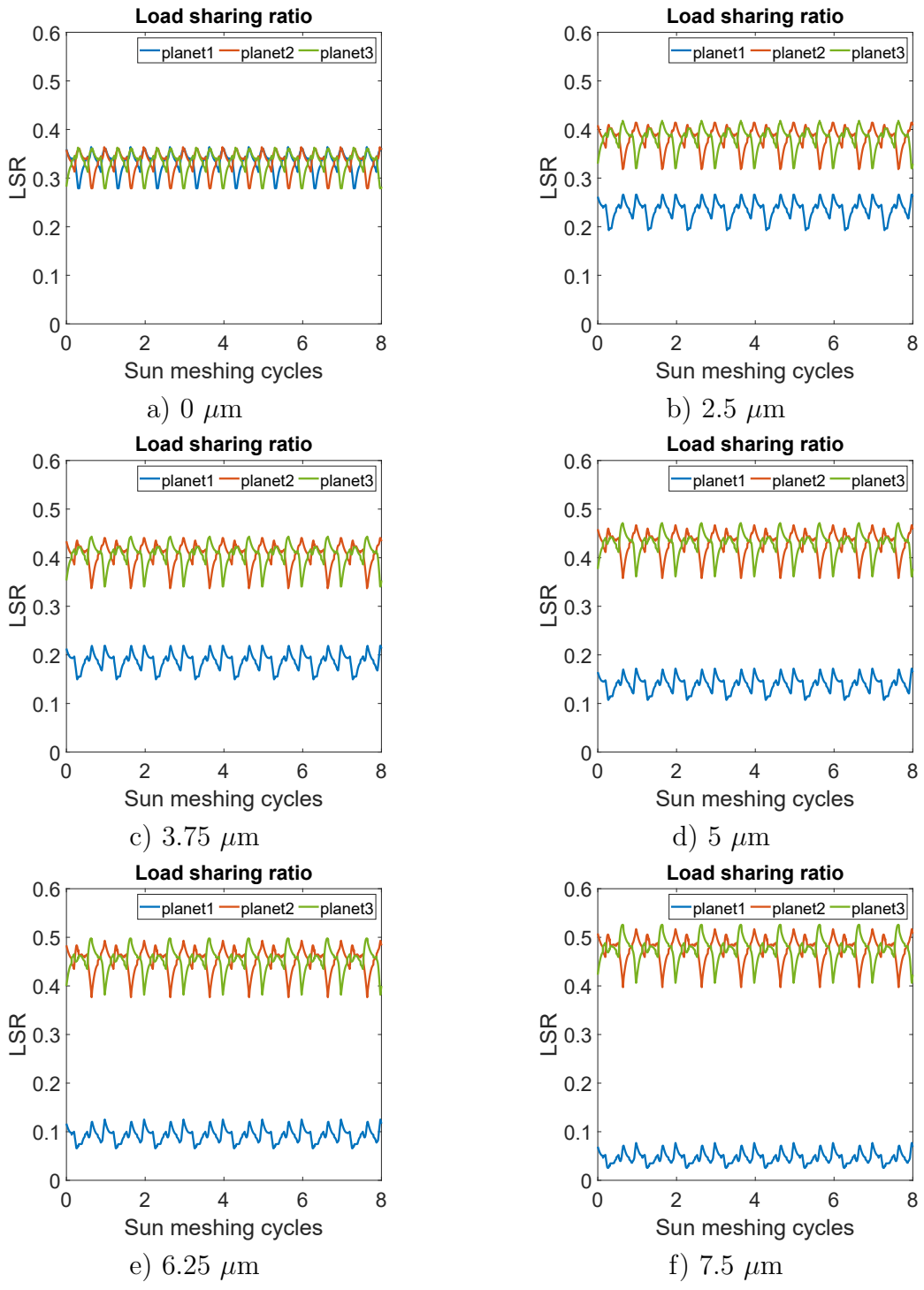


Figure 16: Load Sharing Ratio in ESIP with various errors

2.5-5 there is a higher slope, which changes from then on to a lower slope, even lower than the one in the ESIP transmission's results. Finally, in the last case where there is lost of contact in the planet with error the development of the discrepancy is highly affected, losing any kind of linear proportion with any of the previous values.

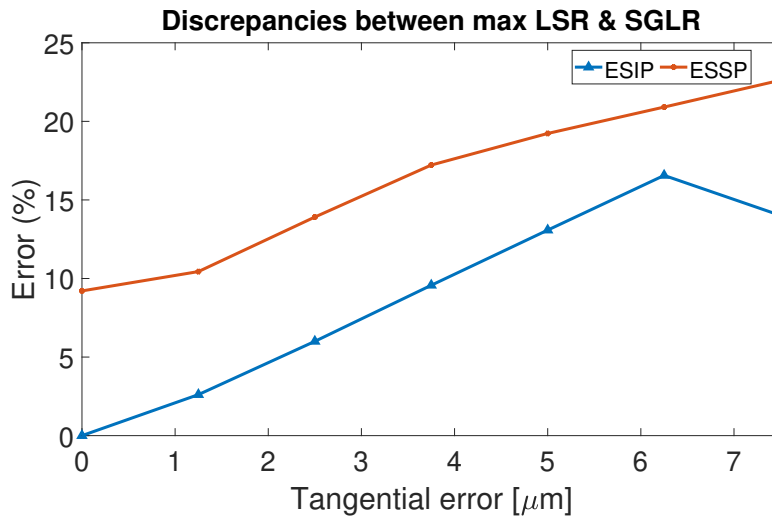


Figure 17: Discrepancies between the maximum LSR and the SGLR results (Graph)

In more depth, in Tab.7 the numerical values of the mentioned discrepancies for every case of study in each planet are gathered. These values prove how the phasing creates a discrepancy in the results, but this discrepancy is uniform for the 3 planets. Then, the tangential error modifies this uniformity. In the ESIP configuration planet 1 behaves differently to planets 2 & 3, who have identical behaviour. On the contrary, in the ESSP transmission the impact of the error is higher and modifies the behaviour of every planet, being the planet 3 the most affected. By this, this planet will be the one that provides the highest inaccuracy in the results obtained by this measuring technique.

Table 7: Discrepancies between maximum LSR and SGLR results (numerical results)

	Planet 1(%)	Planet 2(%)	Planet 3(%)
ESIP@ $e_t$ [0]	0	0	0
ESSP@ $e_t$ [0]	9	9	9
ESIP@ $e_t$ [1.25]	2.31	2.61	2.61
ESSP@ $e_t$ [1.25]	7.44	9.24	10.44
ESIP@ $e_t$ [2.5]	2.97	6	6
ESSP@ $e_t$ [2.5]	6.48	9.36	13.91
ESIP@ $e_t$ [3.75]	3.09	9.57	9.57
ESSP@ $e_t$ [3.75]	5.31	9.87	17.22
ESIP@ $e_t$ [5]	3.24	13.08	13.08
ESSP@ $e_t$ [5]	4.71	11.01	19.23
ESIP@ $e_t$ [6.25]	3.12	16.56	16.56
ESSP@ $e_t$ [6.25]	4.35	12.03	20.91
ESIP@ $e_t$ [7.5]	3	14.01	14.01
ESSP@ $e_t$ [7.5]	3.39	12.51	22.62

## 5. Conclusions

In this section, the conclusions extracted from the results of the proposed study are gathered.

Firstly, the use of strain gauges in the sun gears tooth root to measure the load sharing in planetary transmissions prove to be inaccurate under some conditions. Accuracy is directly affected by the lack of continuous monitoring. This technique just obtains the load sharing for a period of time and therefore, measures only the effects that appear in that time window.

Secondly, the mesh phasing proves to have a crucial impact given the fact that this measuring procedure is not synchronous. Therefore, the synchronization between the strain gauge acquisition and the imbalance-creating factor is crucial in order to obtain the right load sharing measurements by using strain gauges in the sun gear tooth root. In case this synchronization does not exist, the strain gauge would miss the effect of the temporary flaw.

Also, results prove an increment in the error made by the strain gauge with the size of the error. This error is proved to increase at a higher rate than linearly with the size tangential error. The lose of uniformity in the sequence or in the in-phase meshing, produced by the tangential error, proves to play an important role in the measuring technique reliability.

Furthermore, there exists an inherent error by the introduction of a sequence in the meshing. Thus, the calculation procedure to induce the load sharing from the strain gauge data is not appropriate, or if used, some degree of error has to be expected and assumed.

Finally, the influence of the errors accentuate the previously mentioned effect and increment the imbalance in the transmission, as well as the discordance between the results obtained by LSR and strain gauges measurements. The existence of the discrepancies between the results of the two measurements is independent of the transmission studied; the results prove that these inaccuracies appear in any transmission other than an ideal ESIP with no error.

## 6. Acknowledgements

The authors would like to acknowledge Project DPI2017-85390-P funded by the Spanish Ministry of Economy, Industry, and Competitiveness for supporting this research. Moreover, the authors acknowledge the Project PID2020-116213RB-I00 funded by the Ministry of Science and Innovation. Finally, the authors acknowledge SIEMENS-GAMESA for its collaboration in this work.

## References

- [1] A. Kahraman and S. Vijayakar, “Effect of Internal Gear Flexibility on the Quasi-Static Behavior of a Planetary Gear Set,” *Journal of Mechanical Design*, vol. 123, no. 3, p. 408, 2001.
- [2] M. Inalpolat and A. Kahraman, “Dynamic modelling of planetary gears of automatic transmissions,” *Proceedings of the Institution of Mechanical Engineers, Part K: Journal of Multi-body Dynamics*, vol. 222, no. 3, pp. 229–242, 2008.
- [3] Y. Tian, J. Ruan, N. Zhang, J. Wu, and P. Walker, “Modelling and control of a novel two-speed transmission for electric vehicles,” *Mechanism and Machine Theory*, vol. 127, pp. 13–32, sep 2018.
- [4] W. Du, S. Zhao, L. Jin, J. Gao, and Z. Zheng, “Optimization design and performance comparison of different powertrains of electric vehicles,” *Mechanism and Machine Theory*, vol. 156, p. 104143, 2021.
- [5] J. Helsen, F. Vanhollebeke, B. Marrant, D. Vandepitte, and W. Desmet, “Multibody modelling of varying complexity for modal behaviour analysis of wind turbine gearboxes,” *Renewable Energy*, vol. 36, pp. 3098–3113, nov 2011.

- [6] F. Viadero, A. Fernández, M. Iglesias, A. De-Juan, E. Liaño, and M. A. Serna, “Non-stationary dynamic analysis of a wind turbine power drivetrain: Offshore considerations,” *Applied Acoustics*, vol. 77, pp. 204–211, 2014.
- [7] R. G. Parker, V. Agashe, and S. M. Vijayakar, “Dynamic Response of a Planetary Gear System Using a Finite Element/Contact Mechanics Model,” *Journal of Mechanical Design*, vol. 122, no. 3, p. 304, 2000.
- [8] I. Delgado, P. Dempsey, L. Antolick, and D. Wade, “Continued evaluation of gear condition indicator performance on rotorcraft fleet,” in *American Helicopter Society International - Airworthiness, CBM and HUMS Specialists’ Meeting 2013*, pp. 344–365, 2013.
- [9] M. Iglesias, A. Fernandez del Rincon, A. De-Juan, A. Diez-Ibarbia, P. Garcia, and F. Viadero, “Advanced model for the calculation of meshing forces in spur gear planetary transmissions,” *Meccanica*, vol. 50, no. 7, pp. 1869–1894, 2015.
- [10] P. Velez and L. Flamand, “Dynamic Response of Planetary Trains to Mesh Parametric Excitations,” *Journal of Mechanical Design*, vol. 118, no. 1, p. 7, 1996.
- [11] A. Singh, “Load sharing behavior in epicyclic gears: Physical explanation and generalized formulation,” *Mechanism and Machine Theory*, vol. 45, no. 3, pp. 511–530, 2010.
- [12] F. Chaari, T. Fakhfakh, R. Hbaieb, J. Louati, and M. Haddar, “Influence of manufacturing errors on the dynamic behavior of planetary gears,” *The International Journal of Advanced Manufacturing Technology*, vol. 27, pp. 738–746, jan 2006.
- [13] M. Shuai, Z. Ting, J. Guo-guang, C. Xiao-lin, and G. Han-jun, “Analytical investigation on load sharing characteristics of herringbone planetary gear train with flexible support and floating sun gear,” *Mechanism and Machine Theory*, vol. 144, 2020.
- [14] L. Ryali and D. Talbot, “A dynamic load distribution model of planetary gear sets,” *Mechanism and Machine Theory*, vol. 158, 2021.

- [15] C. Zhang, J. Wei, F. Wang, S. Hou, A. Zhang, and T. Lim, “Dynamic model and load sharing performance of planetary gear system with journal bearing,” *Mechanism and Machine Theory*, vol. 151, 2020.
- [16] J. Liu, R. Pang, S. Ding, and X. Li, “Vibration analysis of a planetary gear with the flexible ring and planet bearing fault,” *Measurement*, vol. 165, p. 108100, dec 2020.
- [17] V. Abousleiman and P. Velex, “A hybrid 3D finite element/lumped parameter model for quasi-static and dynamic analyses of planetary/epicyclic gear sets,” *Mechanism and Machine Theory*, vol. 41, no. 6, pp. 725–748, 2006.
- [18] H. Aurrekoetxea, M. Eng, G. Gearbox, I. R. D. Ocenda, E. Eng, and G. Gearbox, “Experimental and theoretical study of Load mesh factor for different boundary conditions in wind gearbox planetary stages,”
- [19] W. Bartelmus and R. Zimroz, “A new feature for monitoring the condition of gearboxes in non-stationary operating conditions,” *Mechanical Systems and Signal Processing*, vol. 23, pp. 1528–1534, jul 2009.
- [20] T. Barszcz and R. B. Randall, “Application of spectral kurtosis for detection of a tooth crack in the planetary gear of a wind turbine,” *Mechanical Systems and Signal Processing*, vol. 23, pp. 1352–1365, may 2009.
- [21] A. Mbarek, A. Del Rincon, A. Hammami, M. Iglesias, F. Chaari, F. Viadero, and M. Haddar, “Comparison of experimental and operational modal analysis on a back to back planetary gear,” *Mechanism and Machine Theory*, vol. 124, pp. 226–247, 2018.
- [22] D. Peng, W. A. Smith, R. B. Randall, and Z. Peng, “Use of mesh phasing to locate faulty planet gears,” *Mechanical Systems and Signal Processing*, vol. 116, pp. 12–24, 2019.
- [23] A. Singh, A. Kahraman, and H. Ligata, “Internal Gear Strains and Load Sharing in Planetary Transmissions: Model and Experiments,” *Journal of Mechanical Design*, vol. 130, no. 7, p. 072602, 2008.

- [24] B. Boguski, A. Kahraman, and T. Nishino, “A New Method to Measure Planet Load Sharing and Sun Gear Radial Orbit of Planetary Gear Sets,” *Journal of Mechanical Design*, vol. 134, no. 7, p. 071002, 2012.
- [25] X. Dai, C. G. Cooley, and R. G. Parker, “Dynamic tooth root strains and experimental correlations in spur gear pairs,” *Mechanism and Machine Theory*, no. 101, pp. 60–74, 2016.
- [26] “IEC61400 – 4: Design Requirements for wind turbine gearboxes.”
- [27] F. L. Litvin and A. Fuentes, *Gear Geometry and Applied Theory*. Cambridge University Press, sep 2004.
- [28] J. Sanchez-Espiga, A. Fernandez-del Rincon, M. Iglesias, and F. Viadero, “Influence of errors in planetary transmissions load sharing under different mesh phasing,” *Mechanism and Machine Theory*, vol. 153, 2020.
- [29] M. Inalpolat and A. Kahraman, “A theoretical and experimental investigation of modulation sidebands of planetary gear sets,” *Journal of Sound and Vibration*, vol. 323, no. 3-5, pp. 677–696, 2009.
- [30] R. G. Parker and J. Lin, “Mesh Phasing Relationships in Planetary and Epicyclic Gears,” *Journal of Mechanical Design*, vol. 126, no. 2, p. 365, 2004.
- [31] K. Weber, C. Banaschek, *The deformation of loaded gears and the effect on their load carrying capacity*. 1951.
- [32] J. Brauer, “A general finite element model of involute gears,” *Finite Elements in Analysis and Design*, vol. 40, pp. 1857–1872, aug 2004.
- [33] H. Ligata, A. Kahraman, and A. Singh, “An Experimental Study of the Influence of Manufacturing Errors on the Planetary Gear Stresses and Planet Load Sharing,” *Journal of Mechanical Design*, vol. 130, no. 4, p. 041701, 2008.
- [34] M. Iglesias, A. Fernandez del Rincon, A. De-Juan, P. Garcia, A. Diez-Ibarbia, and F. Viadero, “Planetary transmission load sharing: Manufacturing errors and system configuration study,” *Mechanism and Machine Theory*, vol. 111, pp. 21–38, 2017.

- [35] A. Kahraman, “Static Load Sharing Characteristics of Transmission Planetary Gear Sets : Model and Experiment,” *Transmission and Driveline Systems Symposium*, no. 1, pp. 1–10, 1999.
- [36] W. Shi, C.-W. Kim, C.-W. Chung, and H.-C. Park, “Dynamic modeling and analysis of a wind turbine drivetrain using the torsional dynamic model,” *International Journal of Precision Engineering and Manufacturing*, vol. 14, pp. 153–159, jan 2013.
- [37] A. Bodas and A. Kahraman, “Influence of Carrier and Gear Manufacturing Errors on the Static Load Sharing Behavior of Planetary Gear Sets,” *JSME International Journal Series C*, vol. 47, no. 3, pp. 908–915, 2004.